Optics and Lasers in Engineering 151 (2022) 106905

Contents lists available at ScienceDirect

Optics and Lasers in Engineering

journal homepage: www.elsevier.com/locate/optlaseng

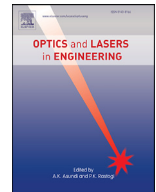

Digital-image-correlation-based thermomechanical diagnostics of Bismuth Telluride pillars in a thermoelectric cooler

Yiyuan Zhang [a], Wenlan Li [a], Zeren Gao [b], Yang Liu [b], Peng Zhang [a,*], Yang Zhao [a,c,*]

[a] CAS Key Laboratory of Mechanical Behavior and Design of Materials and Department of Precision Machinery and Instrumentation, University of Science and Technology of China, Hefei 230026, P.R. China
[b] Department of Modern Mechanics, University of Science and Technology of China, Hefei, Anhui 230027, P.R.China
[c] Key Laboratory of Precision Scientific Instrumentation of Anhui Higher Education Institutes, University of Science and Technology of China

ARTICLE INFO

Keywords:
Thermoelectric cooler
Device reliability
Mechanical damage
Fracture
Thermal stress
Digital image correlation

ABSTRACT

Fatigue-induced fracture of Bi_2Te_3 pillars in a thermoelectric cooler (TEC) due to thermal stress is a prevailing occurrence in the device during dynamic operation, which has been a major reliability concern from manufacturing perspectives. However, it remains a crucial challenge to explore global pillar-level deformation of TEC with simple experiment methodology. Herein, digital-image-correlation-based thermomechanical diagnostics is introduced to experimentally characterize the in-plane thermal deformation of Bi_2Te_3 pillars. Highly contrasted surface pattern generated by He-Ne laser was utilized, exempted from extra speckle fabrication while simultaneously guaranteeing high experimental accuracy. By imposing different thermal loadings to specimen, corresponding full-court pillar-level displacements are respectively observed. Furthermore, shear strain and stress distribution and their dependence on ΔT are studied with stress concentration region identified. The maximum in-plane shear stress at around ΔT= 60 K is indicated to exceed material fracture limit, resulting in high probability of fracture. The good agreement of experimental results and empirical simulation indicates the viability of the proposed technique. Due to its capability of direct observation of thermomechanical behavior of Bi_2Te_3 pillars, the approach employed in this study is of significant practical appeal and notable potential for thermal reliability prediction of thermoelectric device.

1. Introduction

Thermoelectric coolers, as a dependable thermoelectric pathway and key enabler for thermal management of electronics, have earned wide applicability in portable refrigeration, chip-scale cooling of optoelectronic devices, thermoelectric conversion for astronautics, etc [1–4]. The reversible conversion between thermal energy and electricity is commercially effectuated with Bi_2Te_3 alloys as the prominent candidate for the state-of-the-art thermoelectric materials [2–5]. Notably, research attempts at device optimization were continuously focused on the development of thermoelectric materials for decades [6,7].

Nevertheless, the considerable temperature gradients experienced along the Bi_2Te_3 pillars trigger significant thermal stress concentration due to thermal expansion mismatch especially at the junctions of dissimilar material interfaces. Mechanical damages are induced by thermal stress, thus limiting the TEC lifespan (generally 45,000 cycles) and even causing their eventual failure [8]. Since device lifespan also poses a crucial challenge to this cooling strategy, optimized device architecture and enhanced reliability are simultaneously of equal significance to substitute thermoelectric materials [9–13]. Despite the extensive investigations from material perspectives [6,7], relatively less literature reveals the dependence of its thermomechanical performance on device architecture. Trapezoidal thermoelectric pillars were demonstrated instead of rectangular-shaped ones by Merbati et al. [14] for thermal stress distribution analysis and were found to decrease the maximum thermal stress within the devices. Meanwhile, thermomechanical diagnostics is proving its worth for reliability enhancement by researching the thermal stress distribution of TECs and locating stress concentration region within them. However, most thermomechanical diagnostics of TECs have been exclusively based on analytical simulations [15,16]. Thereby, direct experimental investigation of TEC deformation would provide significant insight into the failure prediction of the thermoelectric coolers.

Thermomechanical diagnostics have been experimentally conducted on the TECs like DSPI-based (digital speckle pattern interferometry) investigation by Wang et al. [17], but only out-of-plane thermal displacement of the ceramic package was characterized resultantly. In a previous study by Sun et al. [18,19], in-plane pillar-level rather than package-level deformation was obtained with AFM-DIC method. It should be noted that though the thermally induced deformation was character-

* Corresponding authors.
E-mail addresses: zhp9036@mail.ustc.edu.cn (P. Zhang), yangz1@ustc.edu.cn (Y. Zhao).

https://doi.org/10.1016/j.optlaseng.2021.106905
Received 10 August 2021; Received in revised form 1 November 2021; Accepted 28 November 2021
0143-8166/© 2021 Elsevier Ltd. All rights reserved.

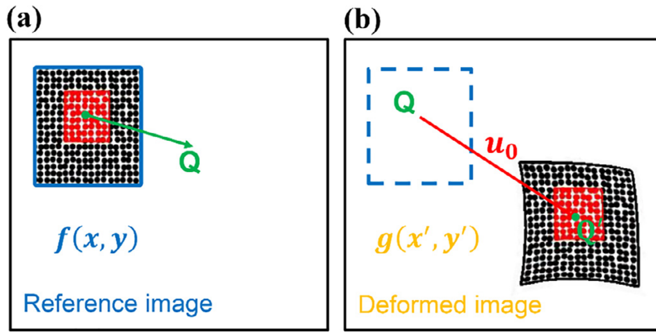

Fig. 1. Principle of digital image correlation.

ized, sophisticated image reconstruction was still required for effective AFM image acquisition, and global distribution of pillar deformation failed to be obtained due to limited measurement range. With the implementation of more advanced digital image correlation (DIC) method, the direct observation of full-court pillar-level deformation can be enabled.

In this work, we present an experimental study of thermomechanical behavior of thermoelectric coolers using DIC technique coupled with images from optical microscopy to measure pillar-level strain field and to verify their durability during heating/cooling thermal loadings. Bi_2Te_3 pillars from a cross-sectioned but fully functional commercial TEC were collimated by laser and observed under optical microscope. High-resolution images of ZOI (zone of interest) were captured and used for deformation calculation with PM Lab software. Highly contrasted surface pattern generated by He-Ne laser was utilized, exempted from extra speckle fabrication while simultaneously guaranteeing high experimental accuracy. By imposing different thermal loadings to specimen, corresponding full-court pillar-level displacements were respectively observed. Based on the resultant displacement fields, shear strain and stress distribution and their dependence on ΔT were studied with stress concentration region identified. Furthermore, the experimental results indicate that the maximum shear stress at ΔT around 60 K exceeds material fracture limit, which agrees with the operation limit given by the user guideline of the device.

2. Principles of DIC technique

Digital image correlation (DIC) is a non-interferometric and non-contacting optical technique with wide applicability to full-field shape, motion and deformation diagnostics [20,21]. The non-contacting feature of this metrology determines its particular adaptability to the characterization of materials that are highly soft, viscoelastic, fragile, or highly brittle like Bi_2Te_3 in this work. The underlying principle of DIC technique is the tracking of graphical points by matching pre- and post-deformed image patterns [22], of which the intensity difference is generated by spraying paint particles or illuminating with collimated laser beam [23]. Broadly, any random intensity distribution with appropriate contrast can serve as a speckle pattern for image matching. As illustrated in Fig. 1, a subset is set up around each pixel respectively, and the post-deformed position of it is then established by subset mapping using pattern matching algorithms. The corresponding points are determined by minimizing the correlation coefficient between the two subset.

Among the prevailing correlation coefficients, Zero-mean Normalized Sum of Squared Differences criterion(ZNSSD) takes into account the linear light intensity changes between images, and is therefore of remarkable adaptability. The correlation function is given as [24]:

$$C_{\mathrm{ZNSSD}}(\Delta p)=\sum_{x=-M}^{M}\sum_{y=-M}^{M}\left[\frac{f(x,y)-f_m}{\sqrt{\sum_{x=-M}^{M}\sum_{y=-M}^{M}\left[f(x,y)-f_{\mathrm{m}}\right]^2}}-\frac{g(x',y')-g_m}{\sqrt{\sum_{x=-M}^{M}\sum_{y=-M}^{M}\left[g(x',y')-g_m\right]^2}}\right]^2 \tag{1}$$

where $f_{\mathrm{m}}=\frac{1}{(2M+1)^2}\sum_{x=-M}^{M}\sum_{y=-M}^{M}f(x,y)$, $g_{\mathrm{m}}=\frac{1}{(2M+1)^2}\sum_{x=-M}^{M}\sum_{y=-M}^{M}g(x',y')$; where $f(x,y)$ denotes the intensity of point $Q(x,y)$ from the reference image, $g(x',y')$ the intensity of the corresponding point $Q'(x',y')$ from the target image, f_{m} and g_{m} are the average intensities of the reference and target subsets respectively, and $p=(u,u_{\mathrm{x}},u_{\mathrm{y}},v,v_{\mathrm{x}},v_{\mathrm{y}})$ is the subset shape vector, in which the subscripts represent the first order derivatives. Hence, a first-order shape function can be defined as [24]:

$$W_1(x,y;p)=\begin{bmatrix}x'\\y'\end{bmatrix}=\begin{bmatrix}1+u_{\mathrm{x}} & u_{\mathrm{y}} & u\\ v_{\mathrm{x}} & 1+v_{\mathrm{y}} & v\end{bmatrix}\begin{bmatrix}x\\y\\1\end{bmatrix} \tag{2}$$

W_1 from Eq. (2) describes the mapping relationship of each point in the subset. Each single pixel from the reference subset is alternately mapped to the post-deformed one to solve for parameter vector p. The inverse compositional Gauss–Newton (IC-GN) iterative algorithm combining with ZNSSD criterion is adopted as optimization strategy in this work for its superiority of computational efficiency over the forward additive Gauss–Newton (FA-GN) algorithm while guaranteeing the same level of accuracy. In each iteration, the incremental warp $W_1(x,y;\Delta p)$ is firstly exerted to the reference subset and subsequently inverted and composed with the current approximation $W_1(x,y;p)$ to update the target subset [24]. Furthermore, Bicubic B-spline interpolation is used to achieve subpixel accuracy.

3. Fabrication and assessment of speckle pattern

The accuracy of digital image correlation (DIC) is strongly dependent on the pattern quality of specimen surface. Therefore, the fabrication of appropriately distributed speckle should be addressed first for DIC experiment. Typically, an ideal pattern should be highly contrasted, stochastic, and isotropic with limited scatter in terms of speckle sizes (averagely 3~5 pixels) [25–27] and also move in synchronous pace with the surface deformation.

When highly coherent laser irradiates a diffusive surface, numerous bright and dark spots, which are called laser speckles, are randomly distributed across the surface [28]. The high-quality speckle pattern generated by laser illumination is captured by CCD as the tracing pattern for DIC. Gao et al. [24] reported that an average $C_{\mathrm{ZNSSD}}(p)$ within 0.05 pixel of ZOI is suitable for calculation. As illustrated in Fig. 2, satisfactory accuracy level of the speckle pattern is achieved with an average $C_{\mathrm{ZNSSD}}(p)$ of 0.002 pixel determined at each 7 pixels of the image. Besides, average noise level is controlled within 1.5548 grayscale. As in the enlarged view of one subset sized 69 pixels, the speckle is averagely sized 3 pixels in sensor format and 3.9 μm in length unit.

4. Experiment

4.1. Experimental setup

A commercially applicative TEC sized 25×25×4.0 mm, supplied by THEMONAMIC CORP, was cross-sectioned while still remaining functional to expose the uppermost row of Bi_2Te_3 pillars as observation target. The sectioning was performed with a high-power Delphi laser and no polishing or any other surface treatment was given afterwards. Spurious effects from vibration were removed by securing the experiment configuration on an optical table. The device was measured in vacuum (0.1Pa) to eliminate the undesired air disturbance, illustrated in Fig. 3(a). Furthermore, the temperature of TEC cold side was sta-

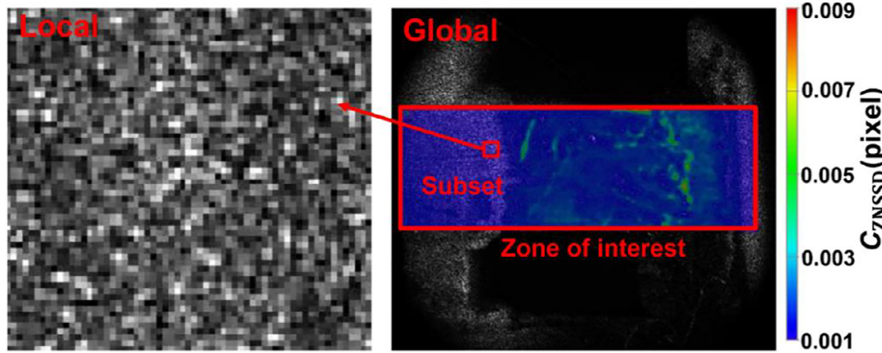

Fig. 2. DIC accuracy analysis of speckle pattern on thermoelectric pillar under microscope (global) and an enlargement of speckle pattern in a subset (local).

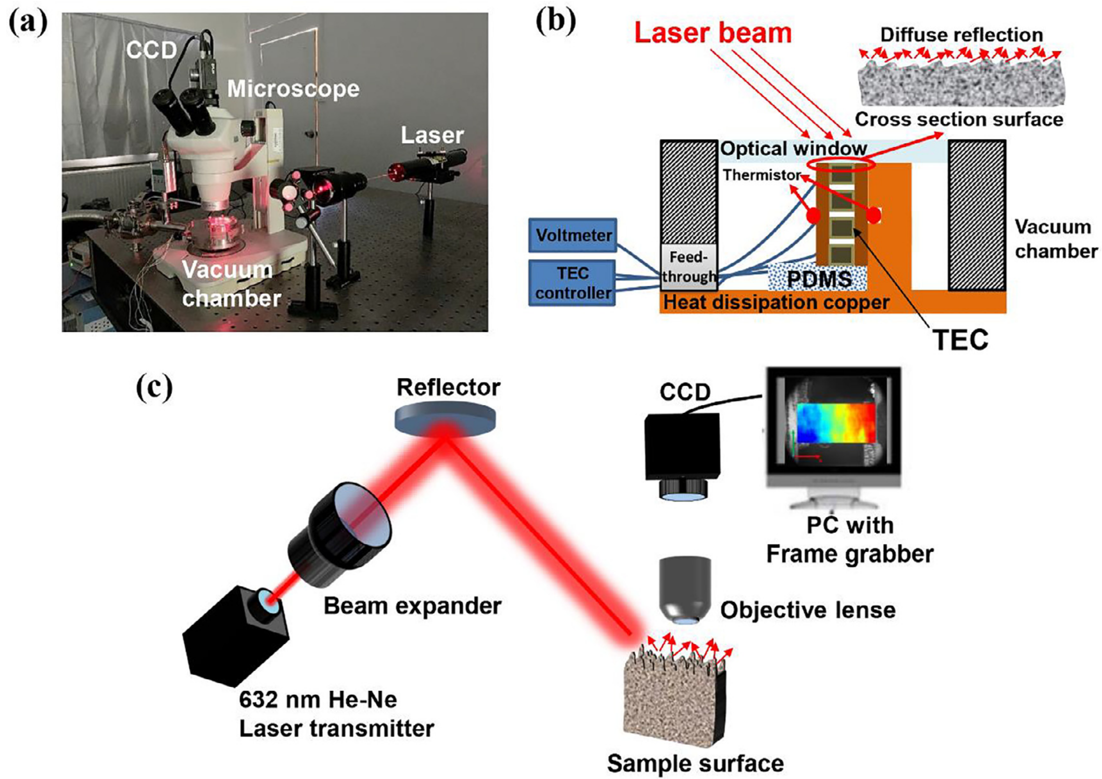

Fig. 3. (a) Experimental setup. (b) Configuration inside the vacuum chamber. (c) Schematic diagram of the optical setup.

bilized using a TEC controller in feedback with a NTC thermistor (10K, 3950) adhered onto its ceramic board. The hot side of the TEC was maintained roughly at room temperature by thermally attached to a copper heat sink. The other thermistor was sandwiched between the ceramic board of the hot side and the copper heat sink to monitor the temperature.

As TEC was energized to generate certain temperature difference, any out-of-plane displacement of the tested surface would result in the change of image magnification thus causing additional pseudo strain. Even worse, it could alter the original laser speckle pattern ruining the effectiveness of image matching. Hence, out-of-plane displacement was minimized to an acceptable level by fitting the pillar surface perfectly with the optical window made of PMMA (polymethyl methacrylate) on the vacuum chamber, as demonstrated in Fig. 3(b). Sample can be practically considered adiabatic with negligible thermal exchange in the normal direction due to vacuum chamber and insignificant thermal conductivity [0.14 W/(m*K)] of PMMA. In practice, TEC was fixed vertically with its underside elastically supported by flexible buffer PDMS (polydimethylsiloxane) with a proper height so that the uppermost pillars extended slightly beyond the sidewall of the chamber. Subsequently the chamber was sealed off with an optical window pressed against the tested pillars firmly. Hence, a basic assumption could be made that there was no obvious out-of-plane displacement on the tested surface of the pillars and was verified in the experiment.

The optical setup used in the present work is illustrated in Fig. 3(c). The sample images were magnified by optical microscope and captured by a high-resolution CCD (pixel dimensions of 3376∗2704) routed to PC display. For the whole setup, the comparison is to be made between the optical resolution and the imaging spatial resolution (1.3 μm).

Optical resolution OR caused by diffraction limit can be determined by [29]:

$$OR = 0.61 * \lambda/NA = 0.61 * 632\,\text{mm}/0.3 = 1.26\,\mu\text{m} \tag{3}$$

where λ denotes the wavelength of emitted laser, NA the numerical aperture objective lens;

The resolution of the integrated imaging system is limited by the smaller of optical resolution and imaging spatial resolution. It can be seen that the optical resolution is slightly less than the imaging spatial

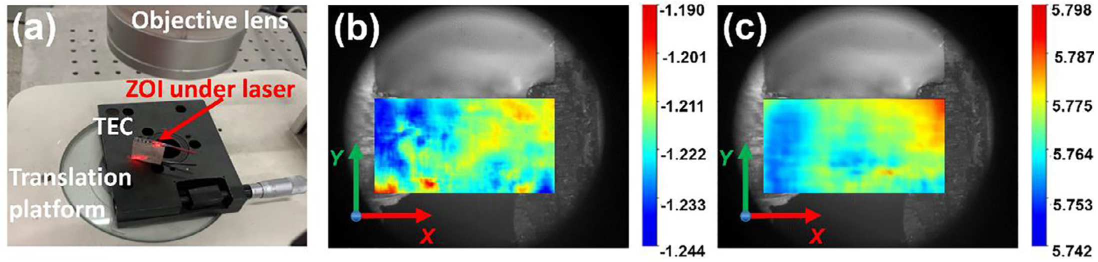

Fig. 4. (a) Calibration system. (b) *u*-displacement and (c) *v*-displacement obtained in the rigid-body translation. (units in μm).

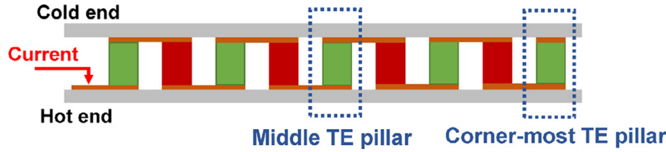

Fig. 5. Middle and corner-most TE pillars observed.

resolution and therefore the resolution of the whole setup is subjected to the limitation of the latter.

4.2. Experiment process

To perform system calibration, a micro-translation platform imposed a rigid-body translation on the sample TEC as in Fig. 4(a), which should yield a uniform displacement field ideally. The imposed *u*-and *v*-displacements are 0.94 and 4.44 pixels respectively. The chosen subset size is 69 pixels and subsets are distributed at an interval of 7 pixels in the zone of interest. The actual displacement field is illustrated in Fig. 4(b) and (c)by cross-correlation of a reference image and a post-image, of which the non-uniformity represents the measurement uncertainty. For a 1.8×1.0 mm ZOI of the pillar with thickness of 1.0 mm, calibration results clearly indicate that the maximum deviation and standard deviation of u-displacement are within 54 nm and 8 nm, which is found at the same level as that of the v-displacement. Hence, the uncertainty of displacement measurement by laser-speckle-based DIC is approximately 0.006 pixel in this study.

The desirable single heating or cooling intervalwas confined to 10 K considering the decorrelation induced by excessive temperature rise or drop. For each stage, the pre- and post-deformation images captured were correlated to explore the deformation of ZOI using PM Lab software [30] supplied by Nanjing PMLAB* Sensor Tech. Co. Ltd. For each temperature stage, 20 images were captured and averaged into one to suppress the noise. The right side of the TEC was its hot end fixed on the heat dissipation copper while the left side was its cold end with a controllable temperature ranging from 273 K to 373 K. The temperature difference of the TEC is defined as: $\Delta T = T_c\text{-}T_h$. Representatively, deformation of the middle pillar and the corner-most pillar in Fig. 5 were both investigated considering that the deformation varies among the pillars.

5. Thermal stress analysis

Thermal stress, triggered by the temperature gradients, intensively occurs where severe mismatch of thermal expansions emerges. Consequent failure of TEC comes with the stress-induced dislocations and cracks. In essential, the magnitude of thermal stress is primarily relevant to displacement, strain, and temperature field. Under the ambient temperature (T_0 = 296 K), the device can be viewed as stress-free, on which any thermally induced deformation in this experiment is based.

It is worth noting that Bi_2Te_3, like most other thermoelectric materials, exhibits no signs of plastic deformation and therefore, no yield strength, similar to ceramic. Given the brittle fracture behavior of this thermoelectric material, assumptions are made that the thermoelectric pillars deform entirely in the range of elasticity without any non-elastic effects such as plasticity or creep.

The normal and the shear strain can be denoted by the in-plane displacement in the displacement-strain relations [15]:

$$\varepsilon_{xx} = \frac{\partial u}{\partial x},\ \varepsilon_{yy} = \frac{\partial v}{\partial y},\ \gamma_{xy} = \frac{1}{2}\left(\frac{\partial u}{\partial x} + \frac{\partial v}{\partial y}\right) \tag{4}$$

Assuming the material is uniform and isotropic, in the plane-strain case where out-of-plane deformation is assumed to be negligible [31], the dimensionless stress-strain constitutive equation is given by a non-symmetrical Jacobian matrix as follows [15]:

$$\begin{Bmatrix}\sigma_x\\ \sigma_y\\ \tau_{xy}\end{Bmatrix} = \frac{E}{(1+v)(1-2v)}\begin{bmatrix}1-v & v & 0\\ v & 1-v & 0\\ 0 & 0 & \frac{1-2v}{2}\end{bmatrix}\left(\begin{Bmatrix}\varepsilon_{xx}\\ \varepsilon_{yy}\\ \gamma_{xy}\end{Bmatrix} - \begin{Bmatrix}\varepsilon_{xx_0}\\ \varepsilon_{yy_0}\\ \gamma_{xy_0}\end{Bmatrix}\right) \tag{5}$$

where E is the Young's Modulus of the material, v the Poisson's Ratio, ε_{xx_0}, ε_{yy_0} and γ_{xy_0} are normal and shear strain due to thermal expansion under stress free condition, which is dependent on temperature difference and thermal expansion coefficient α [15]:

$$\begin{Bmatrix}\varepsilon_{xx_0}\\ \varepsilon_{yy_0}\\ \gamma_{xy_0}\end{Bmatrix} = \begin{Bmatrix}(1+v)\alpha\Delta T\\ (1+v)\alpha\Delta T\\ 0\end{Bmatrix} \tag{6}$$

By substituting Eq. (6) into Eq. (5), the thermal stress distribution can be obtained.

6. Result and discussion

6.1. Displacement field of middle pillar

To characterize the deformation of the middle pillar of the TEC, the cold end of the TEC was subjected to a temperature rise of 12 K from T_0, so that T_c = 308 K and T_h = 296 K. A linear temperature distribution along the pillar can be observed in Fig. 6(c) captured by infrared camera. The resultant displacement fields are shown in Fig. 6(a)-(b) respectively, where *u* and *v* represent the measured displacements in the *x* (horizontal) and *y* (vertical) directions as indicated in the images. Rigid-body displacement and rotation have been removed assuming right side of the TEC to be stationary. Therefore, the maximum displacements in x and y directions occur at the left side of TEC as can be seen in Fig. 6(a)-(b) with u_{max} = 205 nm and v_{max} = 271 nm. The *u*-displacement orients backwards in negative x direction indicating an expansion due to the heating process. The declining displacement amplitude *v* along x direction suggests a sheared motion, which is known as a common failure form of TECs.

6.2. Displacement field of corner-most pillar

It has been analytically affirmed that the highest thermal stress exists in the corner-most thermoelectric pillar [15], where crack of TEC

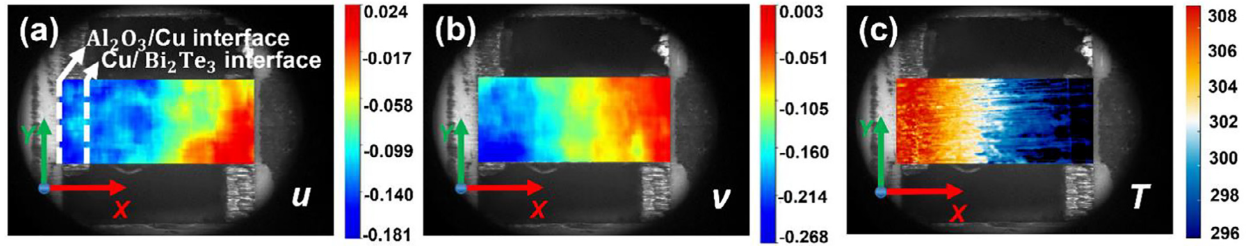

Fig. 6. Temperature and displacement field of the middle TE pillar for heating stage ΔT=12 K. (a) u-displacement and (b) v-displacement for heating stage ΔT=12 K(units in μm). (c) Temperature gradient (units in K).

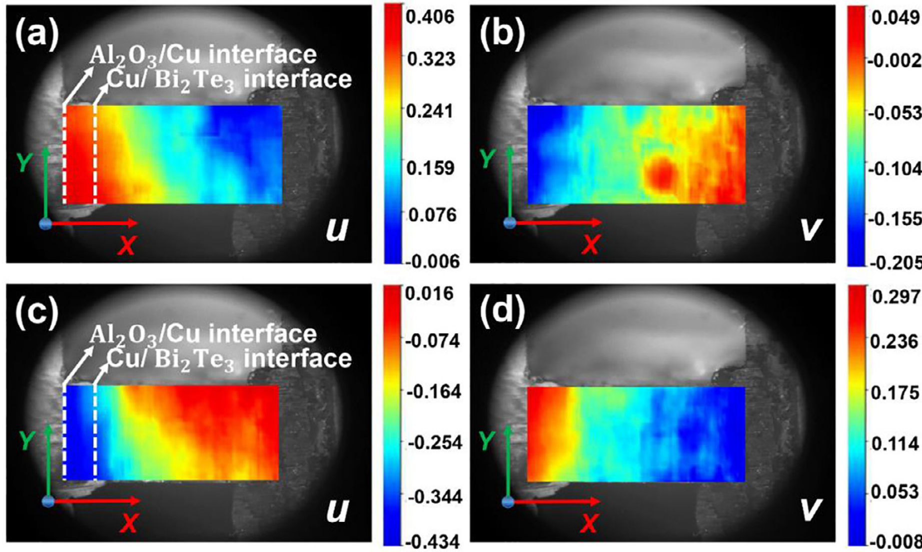

Fig. 7. Displacement field of the corner-most TE pillar. (a) u-displacement and (b) v-displacement for cooling stage ΔT=-10 K. (c) u-displacement and (d) v-displacement for heating stage ΔT=12 K(units in μm).

generally occurs in the first place. Therefore, thermally induced deformation of the corner-most pillar typically indicates device failure and could possibly reveal reliability limit. To quantitatively determine the thermomechanical limit of the entire TEC, the displacement fields of the corner-most pillar for both cooling and heating stages are investigated.

The resultant displacement fields are demonstrated in Fig. 7(a) and (b) for a cooling stage with a T_c drop of 10 K (T_h = 296 K; T_c = 286 K; ΔT = -10 K). With the elimination of the rigid body displacements, it can be seen that the maximum displacement in x direction (u) is 412 nm, and 254 nm in y direction (v). The u-displacement orients forwards in positive x direction since the cold end undergoes cooling-induced shrinkage, while the downward orientation of v-displacement could be understood as the marginal contraction of TEC induced by a negative ΔT. Meanwhile, the shear tendency remains despite the negative ΔT.

Occasions where a TEC is used for heating is by no means less than cooling. To find out the thermomechanical limit of a TEC, displacement fields of the corner-most pillar for heating stage are equivalently crucial as shown in Fig. 7(c) and (d). Similarly, the maximum displacements in x and y directions occur at the left side of TEC with u_{max} = 450 nm and v_{max} = 305 nm. The u-displacement orients backwards more intensively than that of the middle pillar. The upward orientation of v-displacement could be counted as the thermal expansion at the edge of TEC. Furthermore, compared with the middle pillar, the one at corner suffers more deformation as expected.

6.3. Strain field and stress concentration of corner-most pillar

Based on the displacement distribution in both x and y directions, the distribution of strains γ_{xy} can be achieved as illustrated in Fig. 8. It could be found that strain concentration recognizably occurs in the

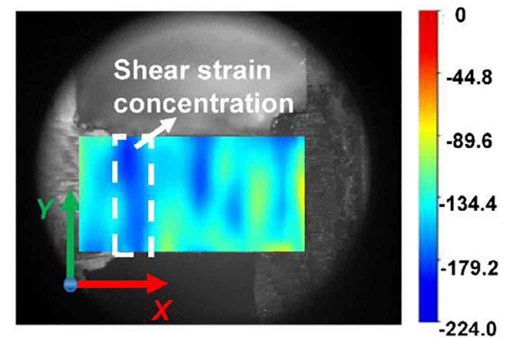

Fig. 8. Shear strain field of the corner-most pillar for heating stage ΔT=12 K. (units in με).

neighboring region of Cu/Bi_2Te_3 interface. Maximum shear strain γ_{max} up to 224 $\mu\varepsilon$ occurs due to the shear motion. Mismatch of the different thermal expansion coefficients results in dislocation of interface and therefore a shear tendency. It is noteworthy that normal strains occur mainly due to thermal expansion induced by ΔT and the corresponding stresses are not obvious.

The material properties within a TEC are listed in Table 1. Negative shear strain τ_{xy} indicates clockwise warping and twisting. From Eq. (5), the shear stress τ_{xy} can be written as:

$$\tau_{xy} = \frac{E}{2(1+\upsilon)}\gamma_{xy} \tag{7}$$

Eq. (7) indicates that the crucial shear stress and the shear strain concentrate at the same location. Therefore, the stress concentration region

Table 1
Properties of major component materials in commercial TEC.

Material	Thermal expansion (/K)	Young's modulus (Pa)	Poisson's ratio
Bi_2Te_3	$-3.11\times10^{-4}+3\times10^{-6}T-1.08\times10^{-8}T^2+1.9\times10^{-11}T^3-1.62\times10^{-14}T^4+5.42\times10^{-18}T^5$	$10^{11}-3.88\times10^{8}T+1.53\times10^{6}T^2-2.666.67T^3+1.67T^4$	0.23
Cu	1.77×10^{-5}	1.19×10^{11}	0.326
Al_2O_3	8.8×10^{-6}	3.5×10^{11}	0.3

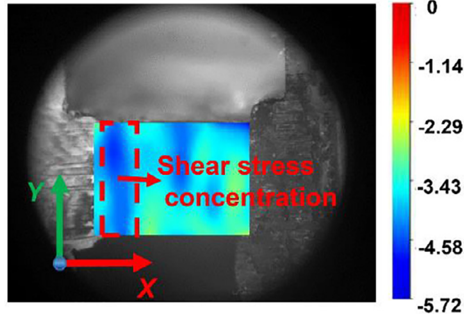

Fig. 9. τ_{xy} shear stress concentration of the corner-most pillar for heating stage ΔT=12 K (units in MPa).

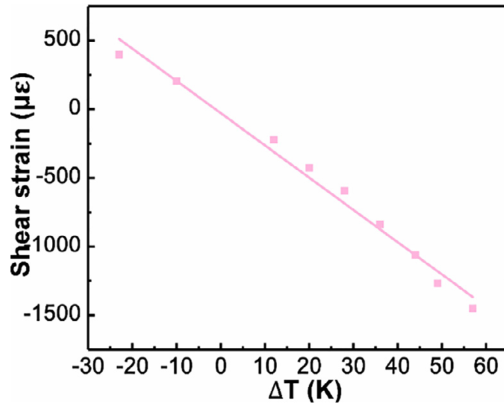

Fig. 10. Maximum shear strain dependence on ΔT.

of functioning thermoelectric pillar can also be determined likewise, as shown in Fig. 9, where the over-load TEC fractures usually occur. For a temperature difference across the pillar ΔT = 12 K, the maximum shear stress τ_{max} is up to 5.72 MPa according to Eq. (7) based on maximum shear strain γ_{max} of 224 $\mu\varepsilon$ and the material properties list in Table 1.

6.4. Maximum strain and stress dependence on ΔT

For commercial TECs, a maximum ΔT of 60 K is common in practice. A thermomechanical diagnostics of Bi_2Te_3 pillars within this temperature range is illustrated in Fig. 10, which basically covers all practical working conditions for regular commercial TECs.

For the Bi_2Te_3 pillar, there is obvious linear correlation between maximum shear strain and ΔT. The fitting curve of γ_{max} basically passes through the origin, which verifies the presumption that device is stress free at initial state (ΔT = 0 K). It can be seen that magnitude of the maximum shear strain γ_{max} is proportional to the temperature gradient, which could reach over 1400 με at ΔT of 57 K.

The actual normal stress would be substantially smaller with little effect on device failure due to the initial normal strain induced by thermal expansions (ε_{xx_0} and ε_{yy_0}) (Eq. (6)). Considering the Bi_2Te_3 pillar is the most vulnerable part of the whole device, device-level thermomechanical limit of TEC can be determined by the pillar-level thermomechanical diagnostics. According to Tresca criterion [31], the failure of

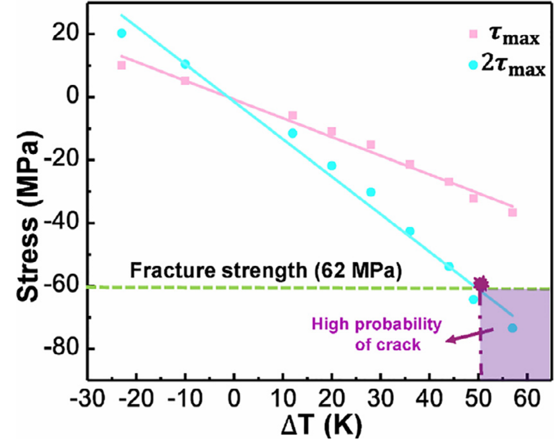

Fig. 11. Shear stress dependence on ΔT.

the device is determined by the maximum shear stress τ_{max}, which can be calculated by:

$$\tau_{max}=\sqrt{\left(\frac{\sigma_x-\sigma_y}{2}\right)^2+\tau_{xy}{}^2} \tag{8}$$

and should satisfy:

$$2\tau_{\mathbf{max}} \le [\sigma] \tag{9}$$

where $[\sigma]$ denotes the fracture strength.

Shear stress τ_{xy} up to 36.7 MPa were measured for the Bi_2Te_3 pillar within common working temperature range of 60 K, which is highly close to empirical simulation results [15]. As illustrated in Fig. 11, the stress level is found to be in linear growth with greater temperature difference, which makes the reliability of TECs predictable.

The doubled maximum shear stress at ΔT = 57 K is found in excess of the fracture strength ($[\sigma]$ =62 MPa) of Bi_2Te_3 [32,33]. It can be estimated from Fig. 11, the probability of fracture is substantially higher when ΔT exceeds 50K. After sufficient TEC operation cycles, stress of this magnitude is likely to trigger continuous device degradation until ultimate failure. The device-level failure is usually indicated by reduction in the figure of merit *ZT*. Substantial degradation of device-level performance will occur (a 20% reduction in *ZT*) at 40,000 thermal cycles before observable defects and eventual fracture of TEC pillars [34]. However, an increase in electrical resistance is actually the primary mechanism of performance degradation, which results from microscopic defects at Cu/Bi_2Te_3 interface due to interfacial contact. The effective figure of merit *ZT* drops by 97% whereas electrical resistance increases by 30% at 45,000 cycles [34]. Therefore, original performance of TEC can hardly be maintained under such high stress level for long. In this regard, TEC performance is simultaneously constrained by not only thermoelectrical but also thermomechanical property of TE material, which reveals the significance of thermomechanical diagnostics of TEC pillars. Briefly, DIC technique based on laser speckle proves applicable for thermomechanical diagnostics of TEC pillar. Ongoing work will be emphasized on alleviating interfacial thermal stresses while guaranteeing good interfacial thermal and electrical conductivity with nanostructured thermal interface materials by this digital-image-correlation-based thermomechanical diagnostics.

7. Conclusion

In this study, a simple and effective laser-speckle-based DIC technique is validated for TEC thermomechanical diagnostics with high displacement accuracy. The proposed method is exempted from complex speckle fabrication and continuity of the displayed displacement fields evince the effectiveness of the laser speckle pattern. The trade-off between adequate sensitivity and sufficient field of view makes this method ideal for global pillar-level scale (1.8×1.0 mm) of common commercial TECs. Furthermore, this DIC-based thermomechanical diagnostics reveals full-court pillar-level deformation distribution and locates the stress concentration region in the neighboring region of Cu/Bi_2Te_3 interface, where fracture is most likely to occur. Meanwhile, thermomechanical behavior of the TEC has been experimentally confirmed by the obvious linear correlation between γ_{max}, τ_{max} and ΔT, which indicates that the magnitude of the shear strain and stress are both proportional to the temperature gradient. Thus, device-level thermomechanical limit of TEC can be determined. Maximum γ_{max} and τ_{max} reach up to 1449 με and 36.7 MPa at ΔT of 57 K, exceeding material fracture limit of Bi_2Te_3, which basically agrees with the operation limit of common commercial thermoelectric coolers. TEC performance is simultaneously constrained by thermoelectrical and thermomechanical property of TE material. This DIC-based thermomechanical diagnostics provides potential prediction of TEC facture behavior and a useful insight to those exploring thermoelectric devices from a design and manufacturing perspective.

Declaration of Competing Interest

The authors declare that they have no known competing financial interests or personal relationships that could have appeared to influence the work reported in this paper.

Acknowledgments

This work was supported by the National Natural Science Foundation of China (#51732006 and #11772321). The authors wish to thank USTC Center of Micro-Nanoscale Research and Fabrication and Experimental Center of Engineering and Material Science of USTC for providing the experimental facilities used in this work.

References

[1] Mao, J., G. Chen, and Z.F. Ren, Thermoelectric cooling materials. Nature Materials: p. 8.
[2] Minnich AJ, et al. Bulk nanostructured thermoelectric materials: current research and future prospects. Energy & Environmental Science 2009;2(5):466–79.
[3] Liu D, et al. Thermoelectric mini cooler coupled with micro thermosiphon for CPU cooling system. Energy 2015;83:29–36.
[4] Majumdar A. THERMOELECTRIC DEVICES Helping chips to keep their cool. Nature Nanotechnology 2009;4(4):214–15.
[5] Martinez A, Astrain D, Aranguren P. Thermoelectric self-cooling for power electronics: Increasing the cooling power. Energy 2016;112:1–7.
[6] Mao J, et al. High thermoelectric cooling performance of n-type Mg3Bi2-based materials. Science 2019;365(6452):495–8.
[7] Pan Y, et al. Mg-3(Bi,Sb)(2)single crystals towards high thermoelectric performance. Energy & Environmental Science 2020;13(6):1717–24.
[8] Cui YJ, Wang BL, Wang KF. Thermally induced vibration and strength failure analysis of thermoelectric generators. Applied Thermal Engineering 2019;160:12.
[9] Kishore RA, et al. Taguchi optimization of bismuth-telluride based thermoelectric cooler. Journal of Applied Physics 2017;122(2):12.
[10] Siddique, A.R.M., S. Mahmud, and B. Van Heyst, Performance comparison between rectangular and trapezoidal-shaped thermoelectric legs manufactured by a dispenser printing technique. Energy, 2020. 196.
[11] Su N, et al. 3D-printing of shape-controllable thermoelectric devices with enhanced output performance. Energy 2020;195:12.
[12] Siddique AM, et al. Performance analysis of bismuth-antimony-telluride-selenium alloy-based trapezoidal-shaped thermoelectric pallet for a cooling application. Energy Conversion and Management 2020;222:12.
[13] Qiu CS, Shi WK. Comprehensive modeling for optimized design of a thermoelectric cooler with non-constant cross-section: Theoretical considerations. Applied Thermal Engineering 2020;176:14.
[14] Al-Merbati AS, Yilbas BS, Sahin AZ. Thermodynamics and thermal stress analysis of thermoelectric power generator: Influence of pin geometry on device performance. Applied Thermal Engineering 2013;50(1):683–92.
[15] Gong TR, et al. *Thermo-mechanical analysis on a compact thermoelectric cooler.* Energy 2019;172:1211–24.
[16] Gong TR, et al. Transient thermal stress analysis of a thermoelectric cooler under pulsed thermal loading. Applied Thermal Engineering 2019;162:7.
[17] Wang WC, Chang YL. Experimental Investigation of Thermal Deformation in Thermoelectric Coolers. Strain 2011;47:232–7.
[18] Sun YF, Pang JHL. AFM image reconstruction for deformation measurements by digital image correlation. Nanotechnology 2006;17(4):933–9.
[19] Sun Y, Pang JHL, Fan W. Nanoscale deformation measurement of microscale interconnection assemblies by a digital image correlation technique. Nanotechnology 2007;18(39).
[20] Zhou P, Goodson KE. Subpixel displacement and deformation gradient measurement using digital image/speckle correlation (DISC). Optical Engineering 2001;40(8):1613–20.
[21] Pan B, Li K. A fast digital image correlation method for deformation measurement. Optics and Lasers in Engineering 2011;49(7):841–7.
[22] Pan B, et al. Two-dimensional digital image correlation for in-plane displacement and strain measurement: a review. Measurement Science and Technology 2009;20(6):17.
[23] Lionello G, Cristofolini L. A practical approach to optimizing the preparation of speckle patterns for digital-image correlation. Measurement Science and Technology 2014;25(10):9.
[24] Gao Y, et al. High-efficiency and high-accuracy digital image correlation for three--dimensional measurement. Optics and Lasers in Engineering 2015;65:73–80.
[25] Chen ZN, et al. Optimized digital speckle patterns for digital image correlation by consideration of both accuracy and efficiency. Applied Optics 2018;57(4):884–93.
[26] Park J, et al. Assessment of speckle-pattern quality in digital image correlation based on gray intensity and speckle morphology. Optics and Lasers in Engineering 2017;91:62–72.
[27] Song JL, et al. Quality assessment of laser speckle patterns for digital image correlation by a Multi-Factor Fusion Index. Optics and Lasers in Engineering 2020;124:15.
[28] Deng LX, et al. Speckle reduction in laser projection based on a rotating ball lens. Optics and Laser Technology 2021;135:9.
[29] Heintzmann R, Cremer C. Laterally modulated excitation microscopy: Improvement of resolution by using a diffraction grating. Conference on Optical Biopsies and Microscopic Techniques III Stockholm, Sweden; 1998.
[30] PM Lab. PMLAB® Sensor Tech. Co. Ltd. Nanjing. P.R.China 2014. Available from https://www.gaosuxiangji.com/products/detail/nid/3822.html.
[31] Leipholz H. Theory of elasticity. Theory of elasticity. Noordhoff Internat Publishing; 1974. ix+400.
[32] Sattar S. Measuring Probability of Failure of Thermoelectric Legs through Lognormal and Weibull Distribution. Journal of Physics: Conference Series 2020;1560:012025 (5 pp.)-012025 (5 pp.).
[33] Liu WS, et al. Current progress and future challenges in thermoelectric power generation: From materials to devices. Acta Materialia 2015;87:357–76.
[34] Barako MT, et al. Thermal Cycling, Mechanical Degradation, and the Effective Figure of Merit of a Thermoelectric Module. Journal of Electronic Materials 2013;42(3):372–81.